Concurrent scale interactions in the far-field of a turbulent mixing layer

O. R. H. Buxton and B. Ganapathisubramani

Citation: Physics of Fluids **26**, 125106 (2014); doi: 10.1063/1.4903970
View online: http://dx.doi.org/10.1063/1.4903970
View Table of Contents: http://scitation.aip.org/content/aip/journal/pof2/26/12?ver=pdfcov
Published by the AIP Publishing

PHYSICS OF FLUIDS **26**, 125106 (2014)

Concurrent scale interactions in the far-field of a turbulent mixing layer

O. R. H. Buxton[1,a] and B. Ganapathisubramani[2]
[1]*Department of Aeronautics, Imperial College London, London, United Kingdom*
[2]*Aerodynamics and Flight Mechanics Research Group, University of Southampton, Southampton United Kingdom*

(Received 4 August 2014; accepted 1 December 2014; published online 22 December 2014)

The interaction between the large- and small-scales in the self-similar region of a nominally two-dimensional planar mixing layer is examined at a centreline Reynolds number $Re_\lambda \approx 260$ (where Re_λ is the Reynolds number based on Taylor microscale). Particle image velocimetry experiments are performed at two different spatial resolutions, one that captures the range from integral scale (L) to Taylor microscale (λ) and the other that captures the range from Taylor microscale to the Kolmogorov length scale (η), simultaneously. It is found that the amplitude of the small-scale fluctuations (scales $< \lambda$) is modulated by the large-scale velocity fluctuations (scales $> \lambda$). Negative large-scale fluctuations (i.e. large-scale fluctuations that are less than the local mean) are found to coincide with regions where an increase in the amplitude of the small-scale fluctuations is found. This amplification effect, of the small-scales by the large-scales, is found to increase with the magnitude of the large-scale fluctuations. By drawing an analogy between the two different spatially resolved datasets and a large eddy simulation it is shown that the turbulent kinetic energy flux to the sub-grid-scales (SGS) is highly sensitive to the alignment between the fluctuating velocity vector and the gradient of the mean shear of the flow. When these two large-scale vectors are perpendicular there is a notable increase in the small-scale turbulent kinetic energy (TKE) flux. This small-scale TKE flux was observed to be influenced by this large-scale alignment even for the smallest scales present, where the correlation between u_1 and u_2 has vanished (SGS scale $< \lambda/8$). © *2014 AIP Publishing LLC.* [http://dx.doi.org/10.1063/1.4903970]

I. INTRODUCTION

Turbulence is known to be a multi-scale problem, in which energy is transferred from the mean flow into turbulent kinetic energy at large-scales and dissipated into heat at the small-scales via a mean cascade of energy from the large- to the small-scales.[1–3] It has long been suggested that the small-scales of turbulent flows are universal, but there is a distinct interaction between the large- and small-scales. Some recent results, primarily in wall-bounded turbulent shear flows, point to the significance of these interactions.[4–9] However, very little information is available on these interactions in other forms of shear flows. In this study, we aim to examine the nature of this interaction between large- and small-scale velocity fluctuations in a turbulent free shear flow.

Winant and Browand[10] stated that "the region between two parallel streams moving at different speeds is the simplest free shear flow which can be considered." The planar mixing layer can be divided into three regions. The first region is characterised by the growth of small amplitude disturbance waves, with the highest growth rate observed at the most unstable frequency due to the Kelvin-Helmholtz instability. In the second region, these waves grow into discrete, Kelvin-Helmholtz roller vortices and the third region sees these vortices interact by rolling around

[a]Author to whom correspondence should be addressed. Electronic mail: o.buxton@imperial.ac.uk

each other and eventually "pairing."[11,12] This mechanism is similar to that observed in other shear flows such as a circular jet.[13] These rollers are observed to pair by amalgamation and co-rotation of neighbouring rollers and far downstream the mixing layer eventually attains a self-similar state in which a broad range of fluctuations from the large-scale rollers down to the dissipative length scales are present.[10,14–19] It is in this self-similar region that we aim to examine the interactions between large- and small-scale velocity fluctuations. Pradeep and Hussain[20] examined the perturbation of Oseen vortices with small-scale fluctuations and observed that low amplitude perturbations were primarily amplified at the periphery of the vortex cores. This study therefore aims to examine the types of interactions that occur between the large roller type vortices and the smaller scale and more random turbulent fluctuations in the self-similar region of a planar mixing layer.

A variety of researchers have examined the small-scales in different types of turbulent flows (for example, Siggia,[21] Kerr,[22] Ruetsch and Maxey,[23] Jiménez *et al.*,[24] Vincent and Meneguzzi,[25] Mullin and Dahm,[26] and Ganapathisubramani *et al.*[27]). Results indicate that the small-scale structures are in the form of "worms" (for enstrophy) surrounded by "sheets" of dissipation. These small-scale structures are approximately 6-10η (where η is the Kolmogorov length scale) in diameter (or thickness) and extend up to the Taylor microscale (λ) in length (or size). Therefore, the size of these structures is substantially smaller than the integral length scale (L) of the flow. Researchers have also noted that these tubes and sheets appear to be concentrated around larger scale structures (that are larger than Taylor microscale). However, the exact nature of this relationship between dissipative scale structures and larger scale flow structures remains unknown.

The study of Bandyopadhyay and Hussain[28] was the first study (and perhaps the only) that presented an examination of the interaction between large- and small-scales in several different shear flows, including wall-bounded shear flows such as boundary layers and free shear flows such as mixing layers, wakes, and jets. The authors examined short time correlations between the low and high frequency components of hot wire time series data. Correlations were made between the low pass filtered (low frequency) time series data with the envelope of the high frequency component and found a significant degree of coupling between the scales across all shear flows. This coupling between the scales was observed to be maximised when the high frequency and low frequency signals were concurrent.

This relationship between the large- and small-scales is of great importance in the application of large-eddy simulations (LES) to turbulent flows. In LES, one separates the motion into small- and large-scales by spatially filtering the velocity field with a kernel[29] and must therefore model the sub-grid-scale (SGS) stresses of the small-scale turbulent fluctuations. Meneveau and Katz[29] extensively reviews the various models that are used and their validity/accuracy in numerical data.

Meneveau[30] acquired single point measurements in order to test a variety of SGS models and using joint moments between filtered velocity and real (measured) SGS stresses enabled both turbulent kinetic energy (TKE) and enstrophy dissipation to be captured over a significant range of filter widths. Subsequent experiments in a turbulent jet,[31] a cylinder wake,[32,33] and a square duct[34,35] have revealed further statistical information on the geometry, alignment tendencies, and intermittency of the SGS turbulence. Further, O'Neil and Meneveau[32] showed that large-scale organised structures within a turbulent free shear flow are shown to have a significant impact on the statistical distribution of SGS TKE dissipation, even at filter scales well inside the inertial range. van der Bos *et al.*[34] examined the effect of the smallest (SGS) scales on the inertial range structures of turbulence using holographic particle image velocimetry (PIV) in a turbulent square duct flow, away from the wall. The separation of scales was achieved by spatially filtering the data with a box filter of size 30 Kolmogorov (dissipative) length scales. It was shown that the SGS stresses had a significant effect on the evolution of the filtered velocity gradients. Additionally, the study showed that commonly used SGS models, such as the Smagorinsky,[36] non-linear and mixed models successfully reproduced the real SGS stress effects in strain dominated regions of the flow but failed in other, rotationally dominated regions.

In this study, we examine the interactions between large- and small-scale velocity fluctuations in the self-similar region of a turbulent mixing layer. PIV experiments are performed at two different spatial resolutions, one that captures the range from the integral length scale (L) to the Taylor microscale (λ) and the other that captures the range from the Taylor microscale to the Kolmogorov

length scale (η), simultaneously. These data are then utilised to explore the interactions between the large- and small-scales.

II. EXPERIMENTAL FACILITY, METHODS, AND DETAILS

The PIV experiments in this study were conducted in the old recirculating water tunnel facility in the Department of Aeronautics at Imperial College London. The facility had a working section of width 700 mm, length 9 m, and the water was filled to a depth of 600 mm. A nominally two dimensional planar mixing layer was produced by means of placing a perforated metal sheet, 50% open area ratio, on one side of a splitter plate of length 1.25 m and thickness, $h = 20$ mm, that was placed just downstream of the water tunnel's contraction. Both boundary layers along the splitter plate were tripped with a 1 mm diameter wire and the boundary layers were given a streamwise distance of 800 mm over which to develop along the splitter plate. The splitter plate had a 4° triangular trailing edge appended to it in order to generate the mixing layer.

The experiments were carried out in the streamwise-cross-stream planes ($x_1 - x_2$ directions). Throughout this paper, (U_1, U_2, U_3) and (u_1, u_2, u_3) denote the instantaneous and the fluctuating velocity components in the streamwise (x_1), cross-stream (x_2), and spanwise (x_3) directions. The quantities denoted within angled brackets, $\langle\cdot\rangle$, represent the ensemble mean.

The inflow condition of the two boundary layers immediately upstream of the 4° trailing edge is presented in Table I. The Reynolds number of the mixing layer based on the convection velocity ($U_c = [U_\infty^{HS} + U_\infty^{LS}]/2$, where U_∞^{HS} and U_∞^{LS} are the freestream velocities on the high- and low-speed sides of the mixing layer, respectively) and the splitter plate thickness is $Re_h = 5020$, and the Reynolds number based on the Taylor microscale is $Re_\lambda \approx 260$ at the centreline of the measurement location. The measurement location was chosen as it was within the self-similar region of the mixing layer, meaning that the turbulence is fully developed, and the mixing layer is not constrained by the sidewall boundary layers, which is the case further downstream in the facility. The centre of this measurement location is approximately 2 m downstream of the splitter plate's trailing edge which corresponds to $100h$. Figure 1 shows the profiles of the planar mixing layer self-similarity function of Pope[37] at two separate streamwise locations within the flow. These profiles are compared to the dataset of Buxton *et al.*[38] which is a direct numerical simulation of the far field of a mixing layer with comparable Reynolds number based on Taylor microscale ($Re_\lambda = 220$ at the centreline). There is a slight discrepancy for this profile but this can be attributed to a lack of statistical convergence due to the fact that it was produced from only three statistically independent snapshots. Nevertheless, the collapse of these profiles (to within the statistical noise) is illustrative of a self-preserving flow.

A customised PIV setup was constructed in order to capture data at two different spatial resolutions simultaneously. The PIV system consisted of a 200 mJ, 532 nm, Nd:YAG laser (*Litron Nano L 200-15*) and four 2048 × 2048 pixel resolution CCD cameras (*TSI PowerView 4M Plus*). Three of the cameras were mounted below the floor of the water tunnel facility and were fitted with Sigma 105 mm lenses with an aperture setting of f/2.8. The final camera was mounted on a carriage above

TABLE I. Table summarising the condition of the two boundary layers immediately upstream of the 4° trailing edge of the splitter plate.

	Low speed side ($._{LS}$)	High speed side ($._{HS}$)
Freestream velocity, U_∞ (ms^{-1})	0.19	0.38
Boundary layer thickness, δ_{99} (mm)	59.4	78.6
Displacement thickness, δ^* (mm)	4.73	8.64
Momentum thickness, θ (mm)	3.25	6.30
Shape factor, H = δ^*/θ	1.45	1.44
$Re_\theta = U_\infty\theta/\nu$	590	2110

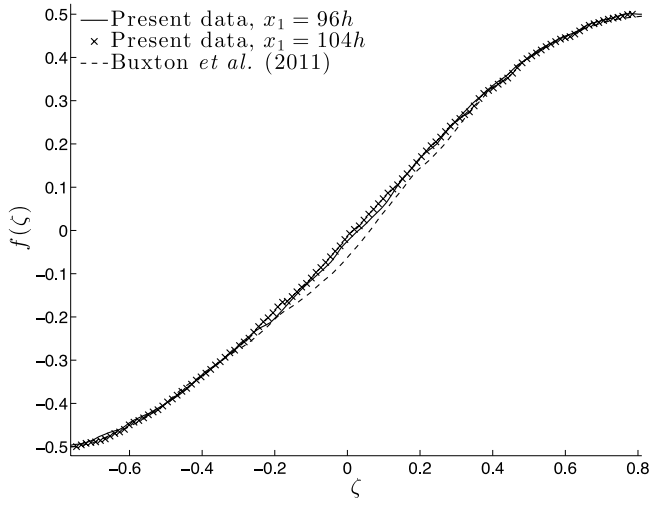

FIG. 1. Profiles of the self-similarity variable, $f(\zeta)$ as a function of ζ (defined in Pope (Ref. 37)) for two separate x_1 locations within the mixing layer. This is overlaid against the direct numerical simulation (DNS) data of Buxton *et al.* (Ref. 38) from a mixing layer at a similar Re_λ.

the water channel and fitted with a Nikon 50 mm lens with an aperture setting of f/2.8. The camera setup is illustrated in Figure 2.

The flow was seeded with polyamide (specific gravity 1.1) particles of diameter 7 μm. In order for the particles to faithfully track the smallest scale fluctuations within the flow, the Stokes number must be less than one, i.e. $St = \tau_R/\tau_F \ll 1$, where τ_R is the response time of the particle and τ_F is the response time of the flow.[39] Since this study is concerned with measuring the dissipative scale fluctuations within the flow, $\tau_F = \tau_\eta = (\nu/\langle\epsilon\rangle)^{1/2}$, i.e. the Kolmogorov time scale which is

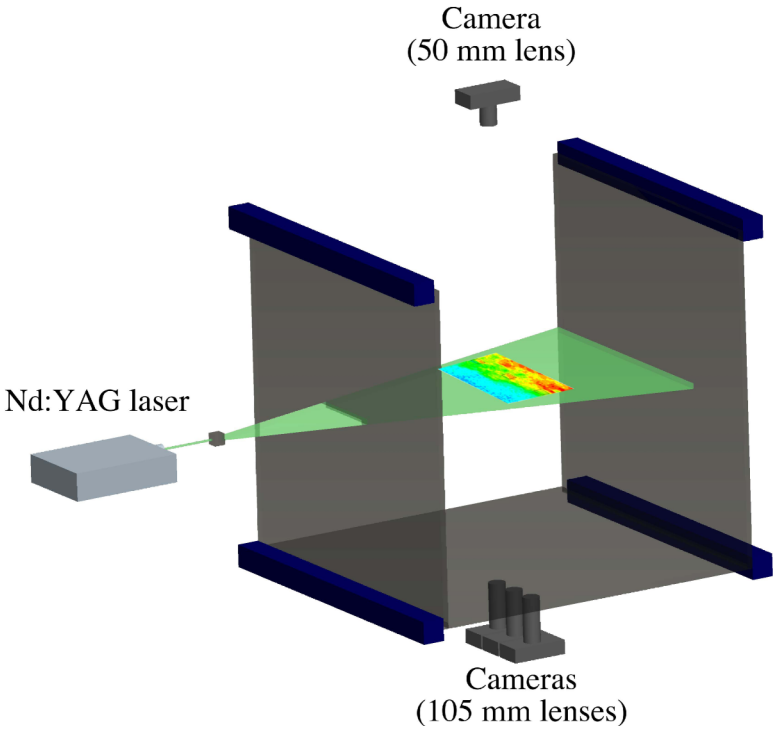

FIG. 2. Schematic of the synchronised PIV setup.

calculated to be 65 ms. Considering very low Reynolds number flow around a sphere, the response time of the particle can be given by $\tau_R = {d_p}^2 \frac{\rho_p}{18\mu}$, where d_p is the particle diameter, ρ_p is the particle density, and μ is the dynamic viscosity of the fluid (water) and is calculated to be 2.6 μs, and hence the $St \ll 1$ condition is comfortably met.

In order to maintain the synchronisation between all four cameras, which were connected via two frame grabbers and were liable to "skip" a frame at higher acquisition rates, and the laser, data were acquired at 0.3 Hz, and immediately written to disk. A suitable separation between the two laser pulses, Δt, for both the top camera (low resolution vector field) and the bottom cameras (high resolution vector fields) was found to be 800 μs, giving a mean streamwise pixel displacement of approximately 25 pixels for the bottom cameras and about 4 pixels for the top camera. Note that this Δt was obtained through a trial-and-error procedure where the objective was to maintain a high quality vector field in the high resolution field of view while maximising the mean pixel displacement in the low resolution field of view.

One thousand image pairs were captured for all four cameras and were processed using the recursive correlation algorithm in the *TSI Insight* software. The initial interrogation area was 128×128 pixels and the final interrogation area was 32×32 pixels for both the top and bottom cameras, with a 50% overlap. A post-processing code was written to validate the vectors and replace spurious ones with either valid secondary peaks or interpolated using a 3×3 local mean technique. The number of spurious vectors was less than 3% in both the high and low resolution fields. Finally, the vectors from both the high and low resolution fields were then interpolated onto a regular Cartesian grid using a bi-linear interpolation method. This was done in order to orient the large-scale Field-Of-View (FOV) to the small-scale fields.

The total field size for the top camera (large-scale field) is 188 mm × 188 mm and is 20.6 mm × 20.6 mm for the bottom cameras (high resolution fields). The spatial resolution for the large-scale field of view is 3.25 mm × 3.25 mm, with adjacent vectors separated by 1.625 mm due to the 50% overlap. The resolution for the small-scale fields of view is 0.37 mm × 0.37 mm (which is comparable to the thickness of the laser sheet), with adjacent vectors separated by 0.19 mm. This is comparable to the sub-Kolmogorov scale resolution achieved in the study of Tanaka and Eaton.[40] Throughout this paper, quantities with the superscript L have been computed from the large-scale low-resolution field of view and quantities with the superscript S have been computed from the small-scale high-resolution fields of view.

As the variation of $\langle \boldsymbol{U} \rangle$ with x_1 is negligible within the large-scale low-resolution FOV, and even more so in the small-scale high-resolution FOVs, mean profiles for each FOV are calculated as a function of x_2 only. Figures 3(a) and 3(b) show the mean streamwise velocity profile and the Reynolds stress profiles, $\langle u_i u_j \rangle$, respectively, at the measurement location (the solid lines are

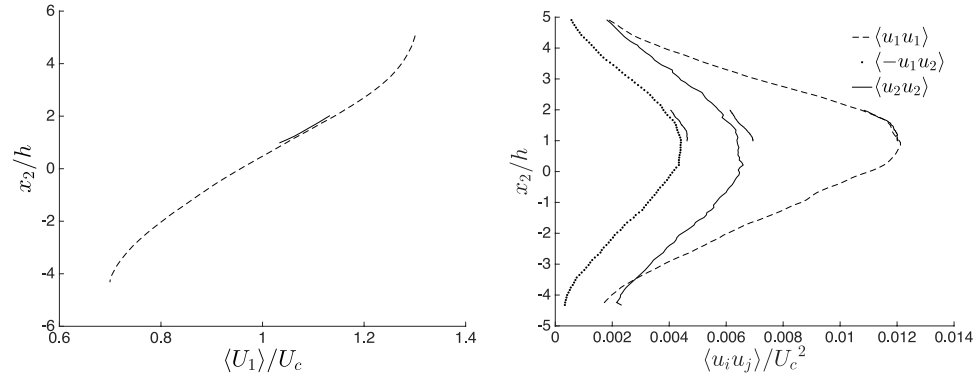

FIG. 3. (a) Mean velocity profile, $\langle U_1 \rangle (x_2)$ for the low-resolution FOV and the high-resolution FOVs at the measurement location (centred at $100h$ downstream of the trailing edge of the splitter plater). (b) Mean Reynolds stress profiles $\langle u_i u_j \rangle$ within the large-scale field of view. The mean and Reynolds stress profiles computed from the high resolution FOVs are shown as solid lines.

computed from the small-scale FOVs). The quantities in Figure 3 are normalised by the convection velocity (U_c) and are clearly typical of a planar mixing layer, c.f. Townsend.[41] The vorticity thickness of the mixing layer, defined as $\delta_\omega = (U_\infty^{HS} - U_\infty^{LS})/\left.\frac{\partial\langle U_1\rangle}{\partial x_2}\right|_{\max}$,[14] is 125.0 mm ($6.25h$). A good agreement is observed between the large- and small-scale FOV data. The three small-scale FOVs are positioned slightly to the high speed side and are therefore just above the peak mean Reynolds stresses, but are nonetheless within an active region very close to the peak.

At the measurement location, the Taylor microscale is calculated to be 10.6 mm and the Kolmogorov length scale, $\eta = \left(\nu^3/\langle\epsilon\rangle\right)^{1/4} = 0.27$ mm, where $\langle\epsilon\rangle$ is the mean rate of dissipation of turbulent kinetic energy. The estimate for the mean rate of dissipation in this study uses the approximation of locally axisymmetric turbulence[42] and the correction method of Tanaka and Eaton.[43] In order to define an appropriate integral length scale (L), separate experiments were performed in which two adjacent cameras were used in the low-resolution configuration in order to compute the auto-correlation function for the streamwise velocity fluctuations. We define the integral scale, L, as the streamwise distance at which the auto-correlation function crosses zero. This was computed to be equal to 222 mm, hence, the streamwise extent of the large-scale FOV is approximately $0.75L$. More details of these experiments can be found in Buxton,[44] including uncertainty estimates and quantification. Table II summarises all the essential experimental parameters at the downstream measurement location.

Figure 4 shows the location of the three high resolution FOVs within the low resolution FOV. The contours are of U_1 and the vectors have components of $(U_1 - U_c)$ and U_2 from the low resolution FOV. The left inset shows contours of U_1 from the low resolution FOV in the region encompassed by the central high resolution FOV and the right inset shows the contours of U_1 from the high resolution FOV itself. It can be seen that there is an excellent agreement between the two. This agreement is further illustrated by the mean profiles from the three high resolution FOVs being superimposed onto the low resolution FOV mean profile in Figure 3(a).

III. SEPARATION OF SCALES AND ANALYSIS PROCEDURES

Figure 5 shows the dissipation spectrum of a turbulent mixing layer at a Taylor Reynolds number that is similar to the one examined in this study, produced from the data of Buxton *et al.*[38] It is observed in this figure that the peak in the dissipation spectrum occurs at or close to the Taylor

TABLE II. Table summarising the experimental condition in the downstream measurement location.

Freestream velocity, U_∞^{HS}	0.38 ms^{-1}
Freestream velocity, U_∞^{LS}	0.19 ms^{-1}
Integral length scale, L	222 mm
Taylor microscale, λ	10.6 mm
Kolmogorov scale, η	0.27 mm
Large-scale FOV	188×188 mm^2
	$0.75L \times 0.75L$
	$18\lambda \times 18\lambda$
	$696\eta \times 696\eta$
Large-scale resolution	3.25 mm
	12η
Small-scale FOVs	20.6×20.6 mm^2
	$0.09L \times 0.09L$
	$1.95\lambda \times 1.95\lambda$
	$76\eta \times 76\eta$
Small-scale resolution	0.37 mm
	1.37η

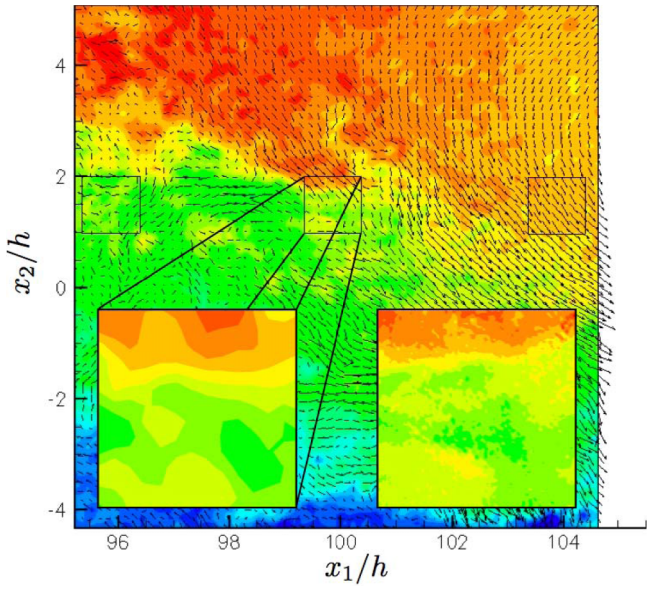

FIG. 4. Example PIV vector fields. The contours are of U_1, the streamwise velocity, and the vectors have components of $(U_1 - U_c)$ and U_2 (with only alternate vectors displayed for ease of presentation), the cross-stream velocity. The insets show a close up of the U_1 contours of the centre high resolution field of view from the low resolution vector field (left) and high resolution vector field (right).

microscale. Therefore, this length scale can thus be considered to "anchor" the dissipation spectrum for this particular flow, hence, λ is considered to be a suitable first estimation for a "cut-off" length scale with which to examine the interaction between the large-scale and small-scale fluctuations.

The large-scale low-resolution FOV is thus filtered to remove all contributions to the fluctuations at length scales smaller than λ (note that this λ is calculated from the small-scale high-resolution FOV). Conversely the small-scale high-resolution FOVs are filtered to remove the contribution of all fluctuations at length scales greater than λ. The additional benefit of implementing a

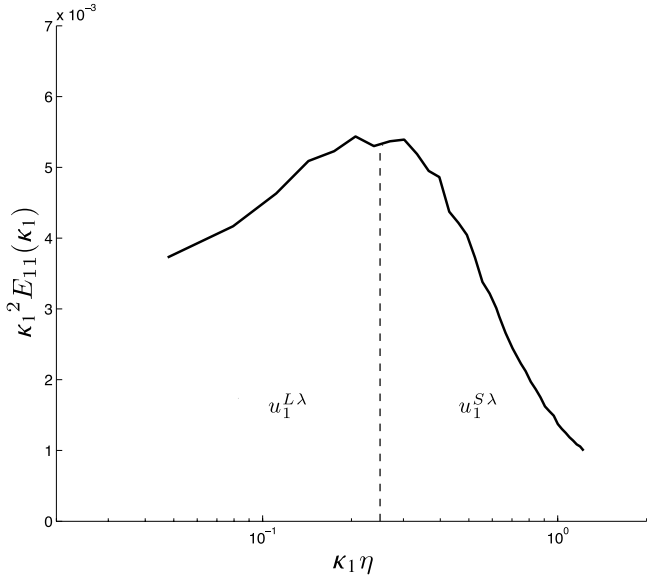

FIG. 5. Dissipation spectrum of the streamwise velocity fluctuations. The vertical lines show the different filters employed to separate the large- ($u_1^{L\lambda}$) and small-scales ($u_1^{S\lambda}$). Data from Buxton *et al.* (Ref. 38).

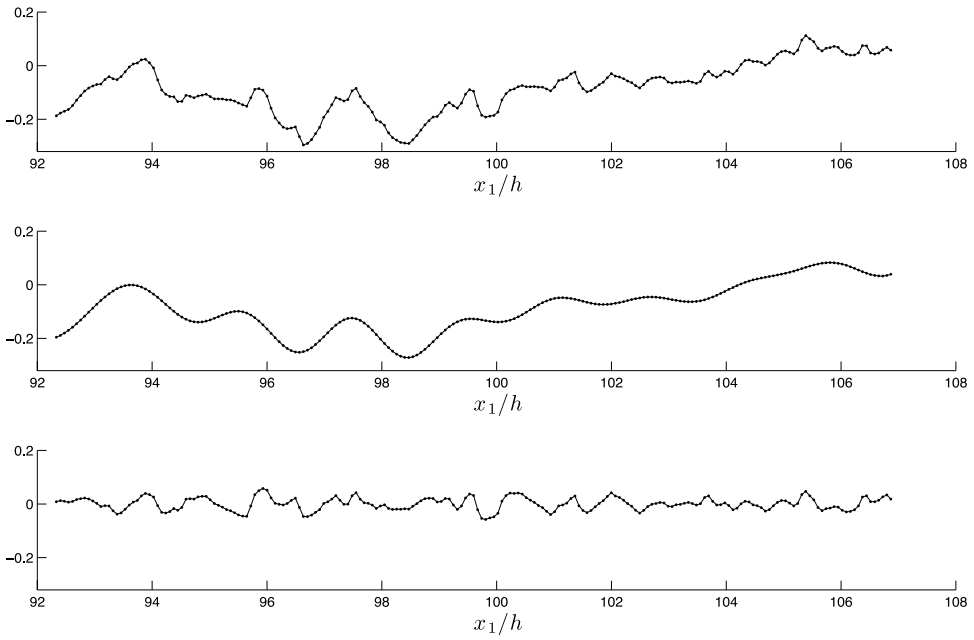

FIG. 6. Top: original signal, $u_1^L(x_1)$. Middle: low wavenumber component of original signal, $u_1^{L\lambda}(x_1)$. Bottom: high wavenumber component of original signal, $u_1^{L0}(x_1)$. $u_1^{L\lambda}(x_1) + u_1^{L0}(x_1) = u_1^L(x_1)$.

low pass filter on the large-scale low-resolution FOV is to eliminate the noisier high wavenumber fluctuations.

The separation of the scales is achieved by means of a running mean filter. It has been previously shown that although a running mean filter does not have a sharp spectral cut-off, the choice of filter has no qualitative effect on the results observed in the modulation of the small-scale fluctuations by the large-scales, and vice versa.[8] The top trace of Figure 6 shows a typical raw signal of $u_1^L(x_1)$ from a low-resolution FOV vector field, the middle trace is the low frequency component of the signal, $u_1^{L\lambda}(x_1)$, and the bottom trace is the part that is composed of fluctuations of length scale λ or less, $u_1^{L0}(x_1)$. The low frequency part and the "$\Lambda < \lambda$" part sum to give the original signal, i.e., $u_1^{L0}(x_1) + u_1^{L\lambda}(x_1) = u_1^L(x_1)$. A similar approach was taken for the small-scale FOV such that $u_1^S = \tilde{u_1^S} + u_1^{S\lambda}$, where $\tilde{\cdot}$ implies convolution with the (running mean) filter kernel, and thus, $u_1^{S\lambda}$ consists of the high frequency content of the small-scale FOV velocity. In a spectral sense, $u_1^{S\lambda}$ can thus be thought of as

$$u_1^{S\lambda} \approx \mathcal{F}^{-1}\left\{U^S(\boldsymbol{\kappa})\right\} \quad \text{where} \quad U^S(\boldsymbol{\kappa}) = \begin{cases} 0 & \forall \quad |\boldsymbol{\kappa}| \leq \dfrac{2\pi}{\lambda} \\ \mathcal{F}\left\{u_1^S\right\} & \forall \quad |\boldsymbol{\kappa}| > \dfrac{2\pi}{\lambda}, \end{cases} \tag{1}$$

where $\mathcal{F}$ denotes the Fourier transform and $\boldsymbol{\kappa}$ is a two dimensional wavenumber vector consisting of components κ_i. This approximation would of course be an equality if a sharp spectral filter was used instead of a running mean filter, however, due to spectral leakage associated with the aperiodicity of PIV data, a running mean filter is instead chosen. The same filter was also applied to the u_2 fluctuations in both the small-scale and large-scale FOVs.

This manuscript presents concurrent analyses representative of the interactions between large- and small-scale fluctuations through conditional statistics. The methodology employed is similar to that employed by Liu *et al.*,[31] and is illustrated in Figure 7. The figure illustrates the stencils for both the large-scale and small-scale FOVs. A region of space that fills a square within the plane of data extending from $-\Delta^L/2$ to $\Delta^L/2$, where Δ^L is the stencil spacing for the large-scale FOV, in both the x_1 and x_2 directions from the (i, j)th node is defined. This region of space will subsequently be referred to as the conditional window. The statistics, whether they be zeroth order,

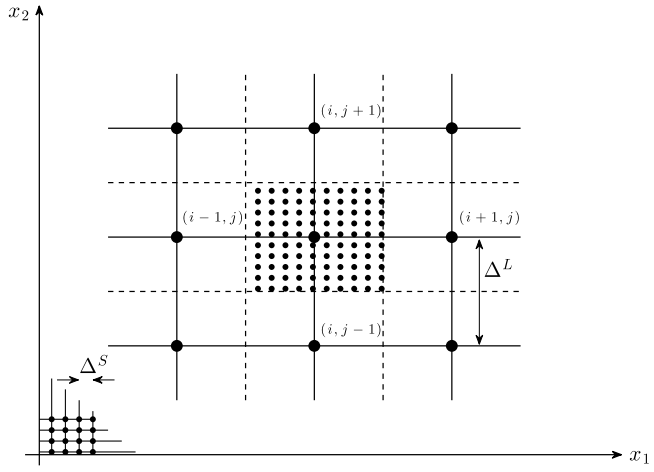

FIG. 7. Schematic illustrating the concurrent grids of the large-scale FOV and small-scale FOV PIV datasets.

first order moments etc., are then conditioned upon the velocity fluctuation of the (i, j)th node of the large-scale FOV data.

In the field of computational fluid dynamics (CFD), a LES is defined as a technique that "consists in solving the set of *ad hoc* governing equations on a computational grid which is too coarse to represent the smallest physical scales."[45] One thus separates the fluid motion into small- and large-scales by spatially filtering the velocity field with a kernel,[29] solving for the large-scales on a coarse grid and modelling the effects of the small (sub-grid) scales. The statistics of the small-scale FOV data within the conditional window can thus be thought of as being analogous to the sub-grid scales of a LES (which are modelled) and the data in the large-scale FOV can be considered to be analogous to the resolved portion.

IV. SCALE INTERACTIONS SEPARATED BY THE TAYLOR LENGTH SCALE

Figure 8 shows conditioned probability density functions (pdfs) of the small-scale fluctuations $u_1^{S\lambda}$ (a) and (b) and $u_2^{S\lambda}$ (c) and (d) conditioned on the sign of the large-scale fluctuations $u_1^{L\lambda}$ (a) and (c) and $u_2^{L\lambda}$ (b) and (d). The small-scale fluctuations are computed as the mean value within the conditional window of a large-scale fluctuation which is typically around 100 small-scale mesh nodes. It can be seen that there is an increased tail in the pdfs along with a reduced modal peak for the case of $u_1^{L\lambda}$ being negative or $u_2^{L\lambda}$ being positive. Evidently, there must be an anti-correlation between u_1 and u_2 since the TKE production term for a free shear flow is $-u_1u_2\partial\langle U_1\rangle/\partial x_2$, which must be positive for the flow to be self-preserving. The correlation coefficient between $u_1^{S\lambda}$ and $u_2^{S\lambda}$ is $\rho_{u_1u_2} = -0.413$, whereas it is $\rho_{u_1u_2} = -0.581$ for the correlation between $u_1^{L\lambda}$ and $u_2^{L\lambda}$. This is reflected in the contrasting effects of concurrent negative $u_1^{L\lambda}$ leading to an increase in small-scale activity and negative $u_2^{L\lambda}$ leading to an attenuation of small-scale activity in comparison to the positive fluctuations.

The location of the small-scale FOV is just to the high speed side of the location of peak Reynolds stresses within the mixing layer. A mechanism whereby a positive $u_2^{L\lambda}$ fluctuation thus brings with it fluid containing an increased level of small-scale turbulent activity can be postulated. This would evidently be coupled to a negative $u_1^{L\lambda}$ due to the requirement that the turbulent flow is self-preserving at the region in which this measurement location is situated. The opposite behaviour is expected in the low speed side of the mixing layer in which case a negative (downwards) $u_2^{L\lambda}$, on average coupled to a positive $u_1^{L\lambda}$, fluctuation will convect with it a region of increased small-scale turbulent activity. This mechanism is perhaps too simplistic though. All of the pdfs of Figure 8 show an asymmetry in which the small-scale activity is preferentially amplified for negative small-scale fluctuations (e.g., $u_1^{S\lambda}$ conditioned on negative $u_1^{L\lambda}$) or positive fluctuations (e.g., $u_2^{S\lambda}$ conditioned on $u_2^{L\lambda}$). The r.m.s. profile of Figure 3, which shows that there is higher turbulent

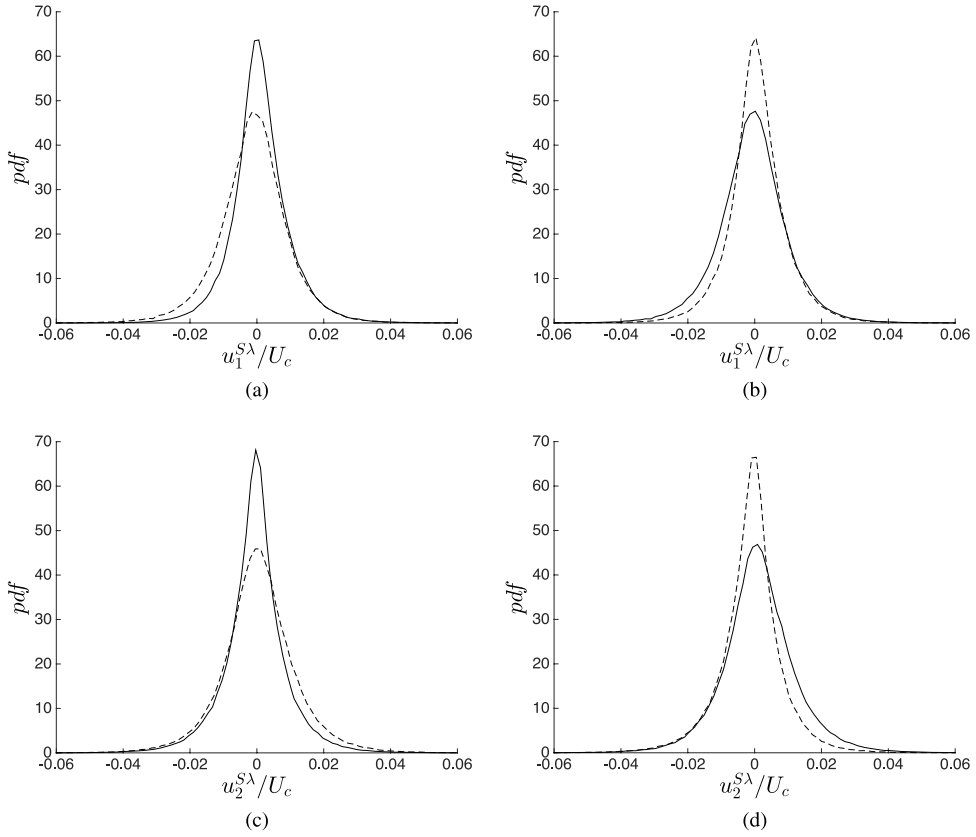

FIG. 8. Probability density functions of the small-scale fluctuations conditioned on the sign of the large-scale fluctuations. (a) $u_1^{S\lambda}$ conditioned on $u_1^{L\lambda}$. (b) $u_1^{S\lambda}$ conditioned on $u_2^{L\lambda}$. (c) $u_2^{S\lambda}$ conditioned on $u_1^{L\lambda}$. (d) $u_2^{S\lambda}$ conditioned on $u_2^{L\lambda}$.

activity to the negative x_2 direction of the small-scale measurement location tells us nothing about the sign of these fluctuations.

Figure 9 illustrates the joint pdfs between the large-scale fluctuations $u_1^{L\lambda}$ and the variance of (a) $u_1^{S\lambda}$ and (b) $u_2^{S\lambda}$. Again, the variance of the small-scale fluctuations is computed from the data present in the conditional windows illustrated in Figure 7. Both figures show that the variance of the small-scale fluctuations, a measure of the "roughness" of the small-scale turbulence, is dependent not only upon the sign of the large-scale fluctuations but also their magnitude. The contours clearly slope from low variance to high variance as the large-scale velocity fluctuation is altered from high

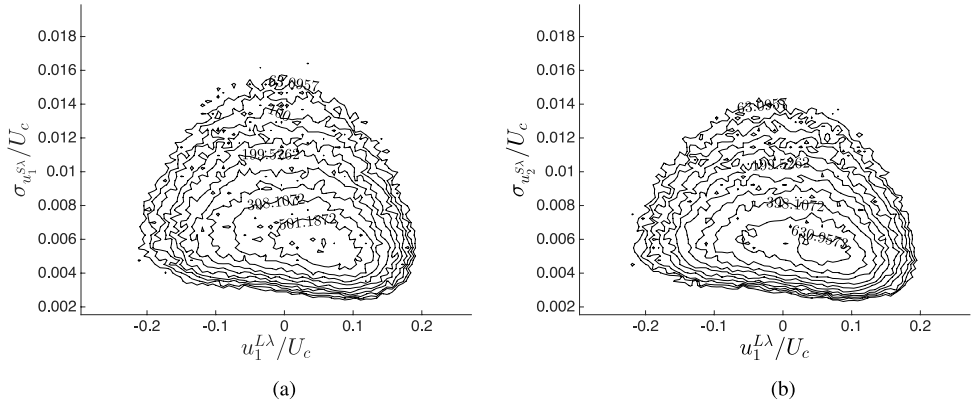

FIG. 9. Joint probability density functions between (a) $\sigma_{u_1^{S\lambda}}$ and (b) $\sigma_{u_2^{S\lambda}}$ and the large-scale u_1 fluctuations.

magnitude positive values (high momentum fluctuation) to high magnitude negative values (low momentum fluctuation). This suggests that not only are negative $u_1^{L\lambda}$ fluctuations concurrent with increased small-scale turbulent activity but also positive $u_1^{L\lambda}$ fluctuations are concurrent with attenuated small-scale activity. The dependence of the small-scale turbulent activity on the magnitude of the large-scale fluctuations and not just the sign, adds further weight to the notion that the convection model for this scale interaction is overly simplistic. Figures 9(a) and 9(b) are both plotted on the same scale, with the same contour levels of the joint pdfs and thus reveal the striking quantitative similarity between the joint pdf between $u_1^{L\lambda}$ and the variance of $u_1^{S\lambda}$ and $u_2^{S\lambda}$. A similar feature is also observed in the amplitude modulation effects of wall bounded flows.[8,9,46]

For a LES, the filtered LES equations for an incompressible flow can be written as

$$\frac{\partial \tilde{\boldsymbol{u}}}{\partial t} + \tilde{\boldsymbol{u}} \cdot \nabla \tilde{\boldsymbol{u}} = -\frac{1}{\rho}\nabla \tilde{p} + \nu \nabla^2 \tilde{\boldsymbol{u}} - \nabla \cdot \boldsymbol{\tau}^{\boldsymbol{\Delta}}, \tag{2}$$

$$\nabla \cdot \tilde{\boldsymbol{u}} = 0, \tag{3}$$

where $\tilde{}$ indicates convolution with the spatial filter employed in the LES, often denoted as $G_\Delta(\boldsymbol{x})$. Equation (2) also includes the term $\nabla \cdot \boldsymbol{\tau}^{\boldsymbol{\Delta}}$, the divergence of the sub-grid scale stress tensor which itself is defined as

$$\tau_{pq}^{\Delta} = \widetilde{u_p u_q} - \tilde{u}_p \tilde{u}_q. \tag{4}$$

Due to the intrinsic closure problem of turbulence τ_{pq}^{Δ} must be modelled, preferably in terms of the resolved velocity field. Since the small-scale fluctuations essentially introduce extra dissipation of TKE, τ_{pq}^{Δ} is often modelled using an "eddy viscosity" model, i.e.,

$$\tau_{pq}^{\Delta} = -2\nu_T \tilde{S}_{pq}, \tag{5}$$

$$\nu_T = \nu_T(\boldsymbol{x}, t), \tag{6}$$

where ν_T is the (artificial) eddy viscosity.

The energy flux to the unresolved sub-grid scales is subsequently given by

$$\Pi(\Delta) = -\tau_{pq}^{\Delta} \tilde{S}_{pq}. \tag{7}$$

If we assume that our coarse grid "cuts off" our fluctuations at a length scale that is within the inertial range of turbulence then the Richardson-Kolmogorov phenomenology implies that there is an equilibrium dissipation meaning that the energy flux transferred to the sub-grid scales is equal to the dissipation rate of those sub-grid scales. That is to say that $\Pi(\Delta) = \epsilon^{\Delta}$.

For this study, we choose an analogue to the small-scale dissipation that avoids a direct computation from the velocity gradient tensor in order to reduce the effect of noise incurred through numerical differentiation of the high-resolution velocity field.[47] "One of the cornerstone assumptions of turbulence theory"[48] is that dissipation can be considered to scale as $\epsilon = C_\epsilon u'^3/L$, where C_ϵ is a constant, u' is the r.m.s. velocity fluctuation, and L is an integral length scale. Converging third order statistics is hard due to the retention of a quantity's sign. This is particularly true when a limited sample of data is available, typically 100 or so small-scale mesh nodes are available for each large-scale mesh node. Instead, we exploit the definition of the Taylor microscale, namely,

$$\lambda^2 = \frac{2u'^2}{\left\langle \left(\frac{\partial u_1}{\partial x_1}\right)^2 \right\rangle}. \tag{8}$$

Further, if we assume that the small-scale velocity gradients are isotropic, which is reasonable since the measurement location is in the self-similar region of the flow, we can estimate the dissipation as

$$\epsilon = 15\nu \left\langle \left(\frac{\partial u_1}{\partial x_1}\right)^2 \right\rangle \tag{9}$$

and thus neglecting numerical coefficients, we obtain

$$\epsilon \sim \nu \left(\frac{u'}{\lambda}\right)^2. \tag{10}$$

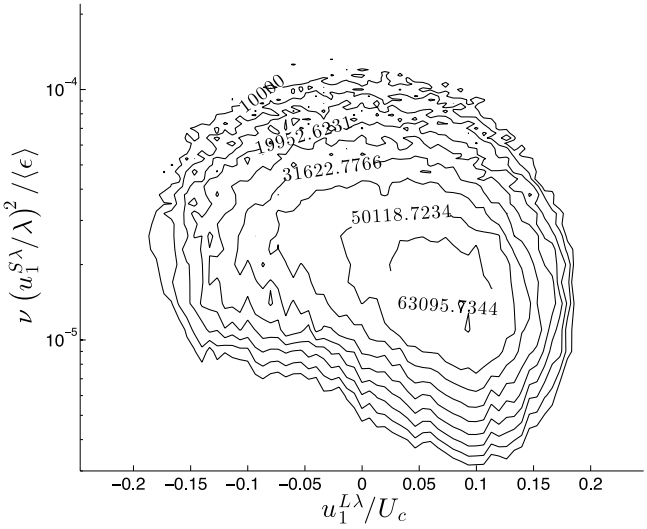

FIG. 10. Joint pdf between the dissipation analogue, $\nu\left(u_1^{S\lambda}/\lambda\right)^2$ and the concurrent large-scale fluctuations.

We thus choose $\nu(u_1^{S\lambda}/\lambda)^2$ as our analogue to dissipation, and hence energy flux to the small-scales, with a higher variance being indicative of "rougher" small-scale turbulence and a higher rate of dissipation resulting from the increased velocity gradients.

The joint pdf between this dissipation analogue and the concurrent large-scale velocity fluctuations is presented in Figure 10. The dissipation analogue is normalised by the mean dissipation rate estimate for the measurement location within this flow which can be seen to be significantly larger than the value of our dissipation analogue. This is due to the fact that Eq. (8) is formulated using the r.m.s. velocity fluctuation, which in the Richardson-Kolmogorov phenomenology of turbulence is dominated by smaller wavenumber components (length scales greater than λ). Nevertheless, our dissipation analogue is dimensionally similar to the dissipation rate and a similar qualitative behaviour is observed to Figure 9. There is a slope in the contours of the joint pdf from lower dissipation concurrent with high magnitude positive fluctuations to higher dissipation concurrent with high magnitude negative velocity fluctuations.

Figure 11 shows pdfs of the small-scale u_1u_2 Reynolds stress component conditioned on the sign of the large-scale fluctuations; (a) $u_1^{L\lambda}$ and (b) $u_2^{L\lambda}$. As mentioned previously, the u_1u_2 component of the Reynolds stress tensor plays the most significant role in the transfer of energy from the mean flow to turbulence in a free shear flow due to its presence in the TKE production term. The majority of TKE production takes place in the large-scales (low wavenumbers) of the Richardson-Kolmogorov phenomenology of turbulence (e.g., Batchelor[49]) however, some TKE production still takes place at smaller length scales. The pdfs are plotted on semi-log axes and it can be seen by virtue of the large focus of data close to $u_1u_2 = 0$ that there is little TKE production at length scales $\Lambda < \lambda$. However, the tails are significantly extended for negative $u_1^{L\lambda}$ / positive $u_2^{L\lambda}$ fluctuations, both the negative and the positive tails. Negative $u_1^{L\lambda}$ fluctuations are thus concurrent with both increased positive and negative TKE production at small (sub-grid) scales.

Tennekes and Lumley[48] noted that there was some evidence to support the notion that vortices whose principal axes were "roughly" aligned with the principle axis of the mean strain in a flow with mean shear are more effective at transferring energy from the mean flow into turbulence. It is thus desirable to see if the same is true for large-scale cross Reynolds stresses $u_1^{L\lambda}u_2^{L\lambda}$. Figure 12 shows the way in which the alignment of the Reynolds stress can be formulated as

$$\theta_{uv} = \arctan\left(\frac{u_2^{L\lambda}}{u_1^{L\lambda}}\right); \quad -\pi \le \theta_{uv} \le \pi. \tag{11}$$

The Reynolds stresses are divided into four quadrants according to the sign of $u_2^{L\lambda}$ and $u_1^{L\lambda}$, similar to the way in which they are categorised in wall bounded flows. For both $u_1^{L\lambda} > 0$ and $u_2^{L\lambda} > 0$, then

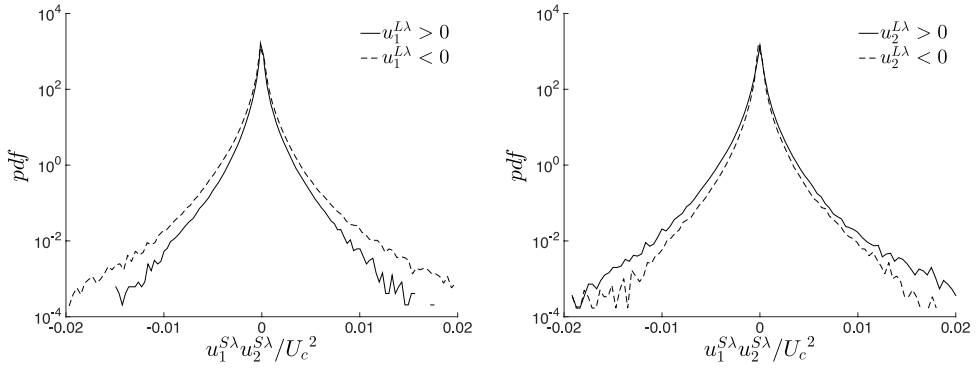

FIG. 11. Probability density functions of the small-scale u_1u_2 Reynolds stress component conditioned on (a) the sign of $u_1^{L\lambda}$ and (b) conditioned on the sign of $u_2^{L\lambda}$.

angle θ_{uv} is bounded by 0 and $\pi/2$ and similarly, for $u_1^{L\lambda} > 0$ and $u_2^{L\lambda} < 0$, known as a "sweep" in wall bounded flows, then θ_{uv} is bounded by 0 and $-\pi/2$. The other two quadrants are categorised as $\pi/2 < \theta_{uv} \leq \pi$ for $u_1^{L\lambda} < 0$ and $u_2^{L\lambda} > 0$, which are known as "ejections" in wall bounded flows, and $-\pi \leq \theta_{uv} < -\pi/2$ for $u_1^{L\lambda} < 0$ and $u_2^{L\lambda} < 0$. The example presented in Figure 12 is of the last kind with both $u_1^{L\lambda} < 0$ and $u_2^{L\lambda} < 0$.

An angle $\theta_{\frac{\partial\langle U_1\rangle}{\partial x_2}}$ can also be formed as the arctangent of the (non-dimensionalised) mean velocity gradient profile (as a function of x_2) and this is also marked onto the figure. Subsequent analyses will present the angle of the large-scale Reynolds stress component relative to this angle $\theta_{\frac{\partial\langle U_1\rangle}{\partial x_2}}$, which will again vary between $-\pi$ and π. Thus, using the example of Figure 12, the angle $\theta_{\frac{\partial\langle U_1\rangle}{\partial x_2}} - \theta_{uv}{}'$ is defined as

$$\theta_{\frac{\partial\langle U_1\rangle}{\partial x_2}} - \theta_{uv}{}' = \theta_{\frac{\partial\langle U_1\rangle}{\partial x_2}} - (2\pi + \theta_{uv}) \tag{12}$$

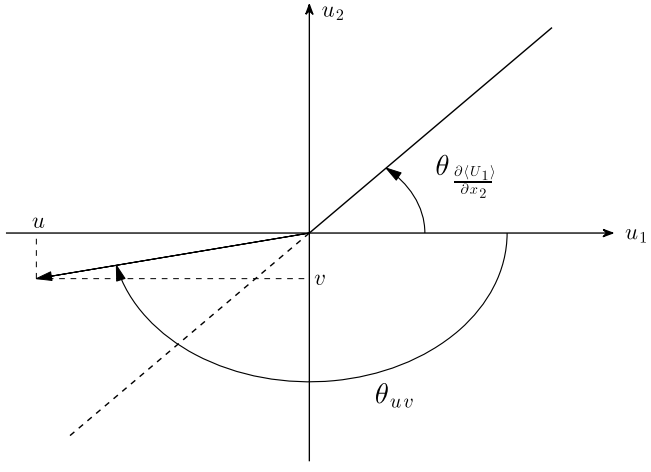

FIG. 12. Schematic illustrating the Reynolds stress angle, θ_{uv} which ranges from $-\pi < \theta_{uv} < \pi$. In the example illustrated, both the u_1 and u_2 fluctuations are negative, with magnitudes u and v, respectively, thereby forming a negative value of θ_{uv}. The angle formed as the arctangent of the cross-stream gradient of the mean velocity profile is marked on as $\theta_{\frac{\partial\langle U_1\rangle}{\partial x_2}}$. In subsequent analyses, the angle formed between $\theta_{\frac{\partial\langle U_1\rangle}{\partial x_2}}$ and θ_{uv} is used. This is also defined as varying from $-\pi$ to π, hence, in the current example, the Reynolds stress angle would be formulated as $2\pi + \theta_{uv}$ thus meaning that $\theta_{\frac{\partial\langle U_1\rangle}{\partial x_2}} - \theta_{uv}$ would be a negative angle whose magnitude is less than (but close to) π.

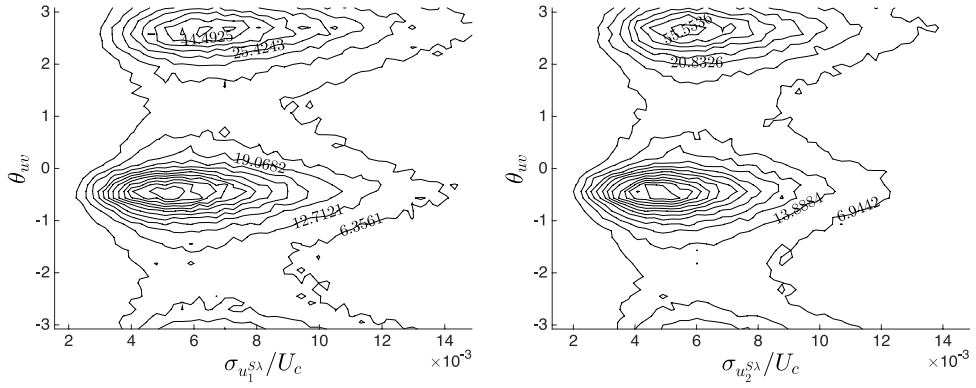

FIG. 13. Joint probability density function between the Reynolds stress angle, θ_{uv} and (a) $\sigma_{u_1^{S\lambda}}$ and (b) $\sigma_{u_2^{S\lambda}}$.

since the reference angle has been rotated by $\theta_{\frac{\partial\langle U_1\rangle}{\partial x_2}}$ in the anti-clockwise (positive) sense. Angles bounded by $-\pi \leq \theta_{\frac{\partial\langle U_1\rangle}{\partial x_2}} - \theta_{uv}{}' < 0$ thus require $\theta_{\frac{\partial\langle U_1\rangle}{\partial x_2}} - \pi \leq \theta_{uv} < \theta_{\frac{\partial\langle U_1\rangle}{\partial x_2}}$, etc.

Figure 13 presents a joint pdf between θ_{uv}, the Reynolds stress angle, and the variance of the small-scale fluctuations, (a) $u_1^{S\lambda}$ and (b) $u_2^{S\lambda}$. It can be seen that the contours are maximised at an angle of $\theta_{uv} \approx -0.47$ ($\approx -27°$), at which angle the contours stretch to a much higher $\sigma_{u_1^{S\lambda}}$ value than at other Reynolds stress angles. There is a second peak located at $\theta_{uv} \approx 2.65$ ($\approx 152°$). The joint pdf is clearly periodic and the second peak, at the positive value of θ_{uv}, can be seen to spill over into the region for which $\theta_{uv} \approx -\pi$. These two peaks, at which there is an observed increase in small-scale activity, are observed to be the same in both Figures 13(a) and 13(b) for the $u_1^{S\lambda}$ and $u_2^{S\lambda}$ fluctuations, respectively. The highest small-scale activity is observed for the peak at the positive angle, i.e., $\theta_{uv} \approx 2.65$. It is clear, however, that no physical significance can be attributed to the Reynolds stress angles associated to maximum small-scale activity other than the fact that they are in anti-phase to one another.

Figure 14 shows the contours of a similar joint pdf to that of Figure 13(a) replacing the Reynolds stress angle with $\theta_{\frac{\partial\langle U_1\rangle}{\partial x_2}} - \theta_{uv}{}'$, which is the Reynolds stress angle relative to the arctangent of the

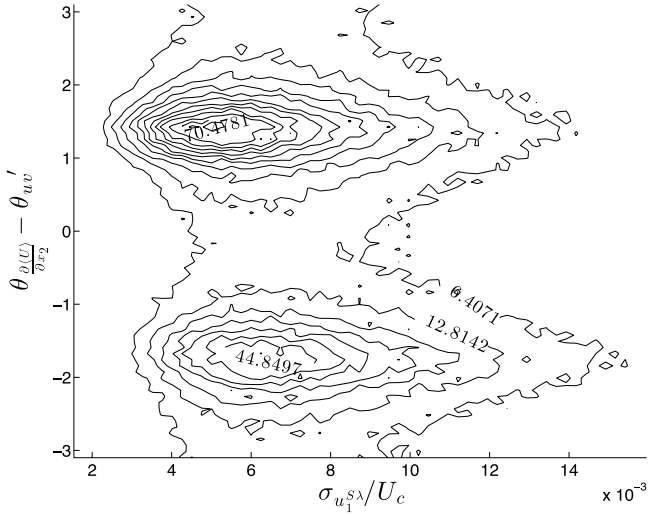

FIG. 14. Joint probability density function between the difference between the Reynolds stress angle, θ_{uv}, and the mean velocity gradient angle and $\sigma_{u_1^{S\lambda}}$.

mean velocity gradient. The contours look similar to those of Figure 13 except that the locations of the peak small-scale activity have been transformed to approximately $\pm\pi/2$. It can thus be concluded that small-scale activity is greatly amplified when the large-scale velocity fluctuation is aligned perpendicularly to the mean velocity gradient of the mixing layer. The highest small-scale activity is observed for $\theta_{\frac{\partial\langle U_1\rangle}{\partial x_2}} - \theta_{uv}{}' \approx -\pi/2$, corresponding to a positive value of θ_{uv}, or an "ejection" event in wall bounded terminology. Whilst Tennekes and Lumley[48] suggested that there was some evidence that vortices whose principal axes are aligned with the mean velocity gradient are more efficient at transferring energy from the mean flow into turbulence, Figure 14 very clearly shows that preferential perpendicular alignment between the Reynolds stress component and the mean velocity gradient leads to a significant amplification of small-scale activity.

V. SCALE DEPENDENCE

The analyses of Sec. IV were focused on the joint and conditioned statistics of the small-scale activity conditioned on the large-scale fluctuations when the scales were separated by the Taylor length scale. Intrinsically, the location at which the large-scales and small-scales are separated is an arbitrary choice; the rationale in Sec. IV was that choosing the Taylor length scale meant that the contribution to the dissipation of TKE was split into two groupings of length scales that contributed similarly to the total dissipation rate, approximately 50% each at this Reynolds number. However, it was noted that the correlation coefficient between $u_1^{S\lambda}$ and $u_2^{S\lambda}$ was $\rho_{u_1u_2} = -0.413$. The significant degree of correlation in the small-scales shows that there is still a contribution to the TKE production term, $-u_1u_2\partial\langle U_1\rangle/\partial x_2$, from fluctuations of length scale less than the Taylor microscale. In order to determine whether there is a non-local scale interaction between large-scales and very small-scales, separated in wavenumber space, it is necessary to observe the effect of filter length on the correlation coefficient $\rho_{u_1u_2}$.

Figure 15 shows a plot of $\rho_{u_1u_2}$ against filter length, Λ, where this is the size of the running mean filter used in order to separate out the smallest scales in the small-scale FOV. Only length scales smaller than Λ are allowed to pass. For comparison, the value of $\rho_{u_1u_2}$ for the large-scales, e.g. $u_1^{L\lambda}$ and $u_2^{L\lambda}$, is -0.581. Typically, a 5% tolerance is required in a miscellany of scientific disciplines before results can be accepted as being statistically significant. Figure 15 shows that for $\Lambda/\lambda = 0.12$, or a filter width of approximately one eighth the Taylor microscale, the (magnitude of the) correlation coefficient between u_1^S and u_2^S falls below the 5% value and can thus be considered to be reflective of $\rho_{u_1u_2} \approx 0$. It should be noted that this filter size is still significantly above the

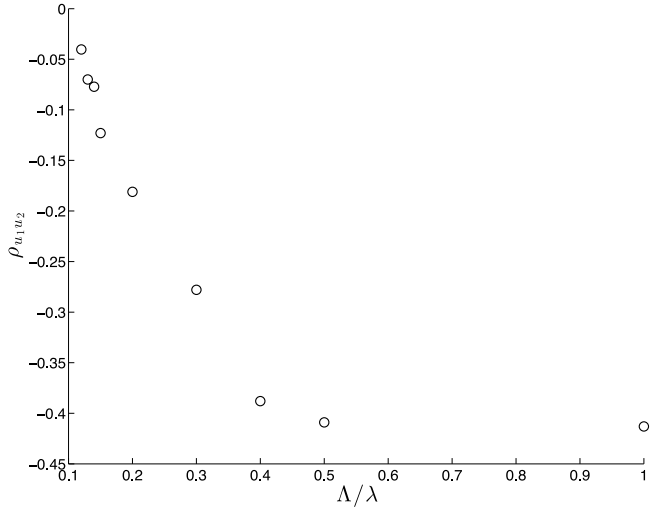

FIG. 15. Correlation coefficient, $\rho_{u_1u_2}$, between u_1^S and u_2^S fluctuations filtered at different length scales, Λ.

noise threshold of the small-scale data, as documented in Buxton,[44] and this lack of correlation is thus not due to the uncorrelated noise dominating but due to the decay of the TKE production term.

Saddoughi and Veeravalli[50] define a correlation coefficient spectrum as outlined in Eq. (13) in which E_{ij} is the power spectral density of $u_i u_j$ and κ_1 is a streamwise wavenumber.

$$R_{12}(\kappa_1) = -\frac{E_{12}(\kappa_1)}{[E_{11}(\kappa_1)E_{22}(\kappa_1)]^{1/2}}. \tag{13}$$

This spectrum is shown to decay to $R_{12}(\kappa_1) \approx 0$ as $\kappa_1 \to \infty$ such that the TKE production term has disappeared for the dissipative range of scales. It is shown that in the range of κ_1 for which a $-5/3$ decay is present for both $E_{11}(\kappa_1)$ and $E_{22}(\kappa_1)$ with κ_1 the spectrum of the correlation coefficient, $R_{12}(\kappa_1)$ is observed to decay with a $-2/3$ slope with respect to κ_1. Whilst Figure 15 is not directly comparable to $R_{12}(\kappa)$ due to the inclusion of all length-scales smaller than filter length Λ it can be seen that there is a clear decay in $\rho_{u_1u_2}$ with Λ. Furthermore, direct comparison between the data of Saddoughi and Veeravalli[50] (in the outer layer of a very high Reynolds number boundary layer, $Re_\lambda \approx 1450$) and the present study shows that for the inertial range the correlation coefficient decays from a value of 0.4 (Eq. (13) is inclusive of the negative sign) to zero. This is matched in Figure 15, with a decay in values of $\rho_{u_1u_2} = -0.413$ to $\rho_{u_1u_2} \approx 0$. Saddoughi and Veeravalli[50] also noted that small-scale anisotropy penetrates to higher κ_1 in flows with a higher mean shear explaining the observation that $\rho_{u_1u_2} \approx 0$ is not observed until $\Lambda = \lambda/8$.

The pdfs of Figure 8 show a difference in the distribution of small-scale fluctuations that lie concurrently with either low momentum (negative) or high momentum (positive) u_1^L fluctuations. A way of quantifying this difference is by means of the Kullback-Leibler divergence (KLD).[51] The KLD, $D_{KL}(P\|Q)$, is a non-symmetric measurement of the difference between two probability distributions and is defined as

$$D_{KL}(P\|Q) = \int_{-\infty}^{\infty} \ln\left[\frac{p(x)}{q(x)}\right] p(x)\,\mathrm{d}x, \tag{14}$$

where $p(x)$ and $q(x)$ are probability density functions of a random variable x. It originated from information theory and can thus be thought of as a loss of information when one tries to model a "true" distribution, $p(x)$, with a modelled distribution, $q(x)$. In general, it does not commute and thus $D_{KL}(P\|Q) \neq D_{KL}(Q\|P)$ and is always non-negative.

Figure 16 shows a plot of the KLD against filter size in which the pdf $p(x)$ is that of the u_1^S fluctuations conditioned on the concurrent large-scale fluctuation being negative, $u_1^{L\lambda} < 0$ and $q(x)$

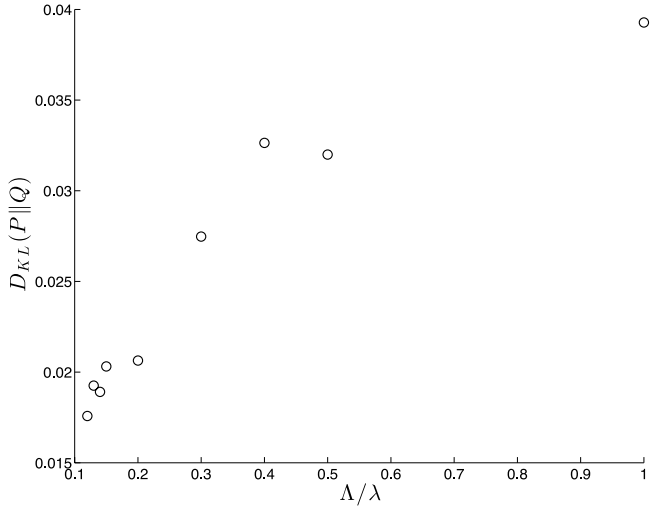

FIG. 16. Kullback-Leibler divergence, $D_{KL}(P\|Q)$ for the difference between pdfs of u_1^S fluctuations conditioned on the sign of u_1^L fluctuations when filtered at various length scales, Λ.

is the *pdf* of the u_1^S fluctuations conditioned on $u_1^{L\lambda} > 0$. It is thus a measure of the loss of information in modelling the *pdf* of the small-scale fluctuations, filtered at length scale Λ, conditioned on negative large-scale fluctuations by the *pdf* conditioned on positive large-scale fluctuations. The decreasing value of KLD as Λ is decreased is thus a consequence of the concurrent large-scale fluctuation having a diminishing effect on the distribution of the small-scale fluctuations at increasingly small length scales. However, the value of the KLD when the filter length is $\Lambda/\lambda = 0.12$ is still approximately 40% that for when the initial demarcation between scales, at the Taylor length scale was used. It is thus clear that the concurrent large-scale fluctuations still influence the small-scale fluctuations even when the correlation between u_1^S and u_2^S has essentially vanished. The mechanism is the same at the smallest scales as it is for the intermediate scales with a concurrent negative $u_1^{L\lambda}$ fluctuation tending to amplify small-scale activity and a concurrent positive $u_1^{L\lambda}$ fluctuation attenuating the small-scale activity.

VI. FURTHER DISCUSSION AND CONCLUSIONS

A series of PIV experiments were carried out in the far-field of a turbulent planar mixing layer within a water tunnel facility that captured large- and small-scale velocity fluctuations simultaneously. The large-scale low-resolution FOV had a resolution of 12η, where η is the Kolmogorov length scale, the small-scale high-resolution FOVs, which are contained within the low-resolution FOV and detailed in Figure 4, had a resolution of 1.3η. In this way, it was possible to resolve the flow field at both the large-scales and the small-scales simultaneously.

The velocity fluctuations within these two fields of view were used to examine the scale interactions in the far-field of turbulent mixing layers. The interaction between two different ranges of scales is explored. First, the fluctuations are separated into large- and small-scale fluctuations using a running mean filter that defines the large-scales as those greater than the Taylor microscale ($u_1^{L\lambda}$) and the small-scales are those that are smaller than the Taylor microscale ($u_1^{S\lambda}$). Conditional *pdf*s were used to investigate the co-dependence of the large- and small-scale fluctuations. The distribution of $u_1^{S\lambda}$ is found to be wider when conditioned on negative large-scale fluctuations than conditioned on positive large-scale fluctuations, and correspondingly, when conditioned upon large-scale fluctuations of the u_2 component of velocity of the inverse sign. This suggests that there is some interaction between the large-scale fluctuations and the small-scale fluctuations, whereby negative large-scale fluctuations tend to magnify the amplitude of the small-scale fluctuations contained within themselves. Similar findings have been found in studies in wall bounded turbulent flows in which the sign of the large-scale fluctuations has been shown to affect the amplitudes of the small-scales.[6,7] This study goes further and shows that both the sign and magnitude of the concurrent large-scale fluctuations are observed to affect the small-scale activity, with high magnitude, positive u_1^L fluctuations leading to an attenuation and high magnitude, negative u_1^L fluctuations leading to an amplification.

The orientation of the large-scale u_1u_2 Reynolds stress component with respect to the mean velocity gradient was observed to be of great significance. When the vector formed by u_1^L and u_2^L is observed to be perpendicular to the mean velocity gradient this was shown to significantly increase the small-scale activity and (analogously) the TKE flux to the smallest scales, with the highest flux only possible in this configuration. A slight increase in the TKE flux was observed for Q4 Reynolds stress events, or "sweeps" in wall bounded terminology.

It was then shown that this effect of amplitude modulation of the small-scales by the large-scales is also present down to significantly smaller length scales than merely the Taylor microscale. The filter length scale at which the correlation between u_1^S and u_2^S fell below 5% was shown to be $\Lambda \approx \lambda/8$. When these fluctuations, which are now purely dissipative and not responsible for the transfer of energy from the mean flow into turbulence, are conditioned on the large-scales (those greater than λ) the same amplification of small-scale activity was found concurrent to negative u_1^L fluctuations. The degree of this interaction was quantified by means of the Kullback-Leibler divergence, which is a measure of information lost in describing a "true" statistical distribution with a modelled one. This KLD was found to be approximately 40% of that for $\Lambda = \lambda$, indicating a reduced

but still appreciable interaction between the large and smallest scales in the flow. It was also shown that the highest TKE flux from these very small-scales to the smallest scales present in the flow was also still overwhelmingly increased when the concurrent large-scale Reynolds stress vector was aligned perpendicularly to the mean velocity gradient of the flow.

As it was shown that the correlation coefficient between the small-scale u_1 and u_2 fluctuations is approximately zero, we may assume that the flow is locally isotropic when viewed at these length-scales. This is a prerequisite for the Kolmogorov[52] theorem of universal scaling of the dissipative scales in turbulence with the kinematic viscosity, ν and the mean dissipation rate, ϵ, only. These results show that the smallest-scales in fact "feel" the large-scale fluctuations in addition to ν and ϵ. The physical mechanism by which this scale modulation manifests itself is unclear from the concurrent results of this study. In order to investigate the cascade of "information" from the large-scales to the small-scales, it is necessary to observe the time/phase lag that maximises these scale interactions which forms the basis of our future work. In this case, it may be possible to link these scale interactions to coherent structures present within the planar mixing layer. The observation of greatly amplified small-scale activity when the large-scale velocity fluctuation is aligned perpendicularly to the mean velocity gradient (Figure 14) is consistent with the ideas of the role of coherent structures in a planar mixing layer presented in Hussain.[53]

ACKNOWLEDGMENTS

Funding from EPSRC through Grant Nos. EP/F056206/1 and EP/I004785/1 as well as the Doctoral Training Grant (for ORHB) is greatly appreciated. ORHB would also like to thank the Royal Aeronautical Society for additional funding.

[1] L. F. Richardson, "Atmospheric diffusion shown on a distance-neighbour graph," Proc. R. Soc. London, Ser. A **110**(756), 709–737 (1926).
[2] G. K. Batchelor and A. A. Townsend, "The nature of turbulent motions at large wave-numbers," Proc. R. Soc. London, Ser. A **199**, 238–255 (1949).
[3] A. N. Kolmogorov, "A refinement of previous hypotheses concerning the local structure of turbulence in a viscous incompressible fluid at high Reynolds number," J. Fluid Mech. **13**, 82–85 (1962).
[4] P. J. A. Priyadarshana, J. C. Klewicki, S. Treat, and J. F. Foss, "Statistical structure of turbulent-boundary-layer velocity - vorticity products at high and low Reynolds numbers," J. Fluid Mech. **570**, 307–346 (2007).
[5] M. Kholmyansky and A. Tsinober, "Kolmogorov 4/5 law, nonlocality, and sweeping decorrelation hypothesis," Phys. Fluids **20**, 041704-1–041704-4 (2008).
[6] R. Mathis, N. Hutchins, and I. Marusic, "Large-scale amplitude modulation of the small-scale structures in turbulent boundary layers," J. Fluid Mech. **628**, 311–337 (2009).
[7] R. Mathis, J. P. Monty, N. Hutchins, and I. Marusic, "Comparison of large-scale amplitude modulation in turbulent boundary layers, pipes and channel flows," Phys. Fluids **21**, 111703 (2009).
[8] B. Ganapathisubramani, N. Hutchins, J. P. Monty, D. Chung, and I. Marusic, "Amplitude and frequency modulation effects in wall turbulence," J. Fluid Mech. **712**, 61–91 (2012).
[9] C. M. de Silva, E. P. Gnanamanickam, C. Atkinson, N. A. Buchmann, N. Hutchins, J. Soria, and I. Marusic, "High spatial range velocity measurements in a high Reynolds number turbulent boundary layer," Phys. Fluids **26**(2), 025117 (2014).
[10] C. D. Winant and F. K. Browand, "Vortex pairing: The mechanism of turbulent mixing-layer growth at moderate Reynolds number," J. Fluid Mech. **63**, 237–255 (1974).
[11] A. K. M. F. Hussain and K. B. M. Q. Zaman, "An experimental study of organized motions in the turbulent plane mixing layer," J. Fluid Mech. **159**, 85–104 (1985).
[12] R. B. Loucks and J. M. Wallace, "Velocity and velocity gradient based properties of a turbulent plane mixing layer," J. Fluid Mech. **699**, 280–319 (2012).
[13] A. K. M. F. Hussain and K. B. M. Q. Zaman, "Vortex pairing in a circular jet under controlled excitation. Part 2. Coherent structure dynamics," J. Fluid Mech. **101**(3), 493–544 (1980).
[14] G. L. Brown and A. Roshko, "On density effects and large structure in turbulent mixing layers," J. Fluid Mech. **64**, 775–816 (1974).
[15] F. H. Champagne, Y. H. Pao, and I. J. Wygnanski, "On the two-dimensional mixing region," J. Fluid Mech. **74**, 209–250 (1976).
[16] P. E. Dimotakis and G. L. Brown, "The mixing layer at high Reynolds number: Large-structure dynamics and entrainment," J. Fluid Mech. **78**, 535–560 (1976).
[17] M. M. Rogers and R. D. Moser, "Direct simulation of a self-similar turbulent mixing layer," Phys. Fluids **6**(2), 903–923 (1994).
[18] Y. Zohar and C. M. Ho, "Dissipation scale and control of fine-scale turbulence in a plane mixing layer," J. Fluid Mech. **320**, 139–161 (1996).
[19] N. D. Sandham and R. D. Sandberg, "Direct numerical simulation of the early development of a turbulent mixing layer downstream of a splitter plate," J. Turbul. **10**(1), 1–17 (2009).

[20] D. S. Pradeep and F. Hussain, "Effects of boundary condition in numerical simulations of vortex dynamics," J. Fluid Mech. **516**, 115–124 (2004).
[21] E. D. Siggia, "Numerical study of small-scale intermittency in three-dimensional turbulence," J. Fluid Mech. **107**, 375–406 (1981).
[22] R. M. Kerr, "Higher-order derivative correlations and the alignment of small-scale structures in isotropic numerical turbulence," J. Fluid Mech. **153**, 31–58 (1985).
[23] G. R. Ruetsch and M. R. Maxey, "Small-scale features of vorticity and passive scalar fields in homogeneous isotropic turbulence," Phys. Fluids A **3**(6), 1587–1597 (1991).
[24] J. Jiménez, A. A. Wray, P. G. Saffman, and R. S. Rogallo, "The structure of intense vorticity in isotropic turbulence," J. Fluid Mech. **255**, 65–90 (1993).
[25] A. Vincent and M. Meneguzzi, "The dynamics of vorticity tubes in homogeneous turbulence," J. Fluid Mech. **258**, 245–254 (1994).
[26] J. A. Mullin and W. J. A. Dahm, "Dual-plane stereo particle image velocimetry measurements of velocity gradient tensor fields in turbulent shear flow II. Experimental results," Phys. Fluids **18**, 035102 (2006).
[27] B. Ganapathisubramani, K. Lakshminarasimhan, and N. T. Clemens, "Investigation of three-dimensional structure of fine-scales in a turbulent jet by using cinematographic stereoscopic PIV," J. Fluid Mech. **598**, 141–175 (2008).
[28] P. R. Bandyopadhyay and A. K. M. F. Hussain, "The coupling between scales in shear flows," Phys. Fluids **27**(9), 2221–2228 (1984).
[29] C. Meneveau and J. Katz, "Scale-invariance and turbulence models for large-eddy simulation," Annu. Rev. Fluid Mech. **32**, 1–32 (2000).
[30] C. Meneveau, "Statistics of turbulence subgridscale stresses: Necessary conditions and experimental tests," Phys. Fluids **6**(2), 815–833 (1994).
[31] S. Liu, C. Meneveau, and J. Katz, "On the properties of similarity subgrid-scale models as deduced from measurements in a turbulent jet," J. Fluid Mech. **275**, 83–119 (1994).
[32] J. O'Neil and C. Meneveau, "Subgrid-scale stresses and their modelling in a turbulent plane wake," J. Fluid Mech. **349**, 253–293 (1997).
[33] S. Cerutti and C. Meneveau, "Statistics of filtered velocity in grid and wake turbulence," Physics of Fluids **12**(5), 1143–1165 (2000).
[34] F. van der Bos, B. Tao, C. Meneveau, and J. Katz, "Effects of small-scale turbulent motions on the filtered velocity gradient tensor as deduced from holographic particle image velocimetry measurements," Phys. Fluids **14**(7), 2456–2474 (2002).
[35] B. Tao, J. Katz, and C. Meneveau, "Statistical geometry of subgrid-scale stresses determined from holographic particle image velocimetry measurements," J. Fluid Mech. **457**, 35–78 (2002).
[36] J. Smagorinsky, "General circulation experiments with the primitive equations. I. The basic experiment," Mon. Weather Rev. **91**(3), 99–164 (1963).
[37] S. B. Pope, *Turbulent Flows* (Cambridge University Press, 2000).
[38] O. R. H. Buxton, S. Laizet, and B. Ganapathisubramani, "The interaction between strain-rate and rotation in shear flow turbulence from inertial range to dissipative length scales," Phys. Fluids **23**, 061704 (2011).
[39] M. Raffel, C. E. Willert, S. Wereley, and J. Kompenhans, *Particle Image Velocimetry - A Practical Guide*, 2nd ed. (Springer-Verlag, 2007).
[40] T. Tanaka and J. K. Eaton, "Sub-Kolmogorov resolution particle image velocimetry measurements of particle-laden forced turbulence," J. Fluid Mech. **643**, 177–206 (2010).
[41] A. A. Townsend, *The Structure of Turbulent Shear Flow*, 2nd ed. (Cambridge University Press, 1976).
[42] W. K. George and H. J. Hussein, "Locally axisymmetric turbulence," J. Fluid Mech. **233**, 1–23 (1991).
[43] T. Tanaka and J. K. Eaton, "A correlation method for measuring turbulent kinetic energy dissipation rate by PIV," Exp. Fluids **42**, 893–902 (2007).
[44] O. R. H. Buxton, "Fine scale features of turbulent shear flows," Ph.D. thesis (Imperial College London, 2011).
[45] P. Sagaut, *Large Eddy Simulation for Incompressible Flows*, 3rd ed. (Springer, Heidelberg, Germany, 2006).
[46] M. Guala, M. Metzger, and B. J. McKeon, "Interactions within the turbulent boundary layer at high Reynolds number," J. Fluid Mech. **666**, 573–604 (2011).
[47] R. J. Hearst, O. R. H. Buxton, B. Ganapathisubramani, and P. Lavoie, "Experimental estimation of fluctuating velocity and scalar gradients in turbulence," Exp. Fluids **53**(4), 925–942 (2012).
[48] H. Tennekes and J. L. Lumley, *A first Course in Turbulence* (MIT Press, Cambridge, MA, 1972).
[49] G. K. Batchelor, *The Theory of Homogeneous Turbulence* (Cambridge University Press, New York, NY, 1953).
[50] S. G. Saddoughi and S. V. Veeravalli, "Local isotropy in turbulent boundary layers at high Reynolds number," J. Fluid Mech. **268**, 333–372 (1994).
[51] S. Kullback and R. A. Leibler, "On information and sufficiency," Ann. Math. Stat. **22**(1), 79–86 (1951).
[52] A. N. Kolmogorov, "The local structure of turbulence in incompressible viscous fluid for very large Reynolds numbers," C. R. Acad. Sci. URSS **30**(4), 301–305 (1941).
[53] A. K. M. F. Hussain, "Coherent structures and turbulence," J. Fluid Mech. **173**, 303–356 (1986).